Modularity in the Organization of Mouse Primary Visual Cortex

Weiqing Ji[1,4], **Rǎzvan Gǎmǎnu**[2,3,4], **Pawan Bista**[1], **Rinaldo D. D'Souza**[1], **Quanxin Wang**[1,5], and **Andreas Burkhalter**[1,*]

[1]Department of Anatomy and Neurobiology, Washington University School of Medicine, 660 South Euclid Avenue, St. Louis, Missouri, 63110, USA

[2]Stem Cell and Brain Research Institute, INSERM U846, 69500 Bron, France

[3]Université Claude Bernard Lyon, 69003 Lyon, France

[5]Allen Institute for Brain Science, Seattle, Washington 98103, USA

SUMMARY

Layer 1 (L1) of primary visual cortex (V1) is the target of projections from many brain regions outside of V1. We found that inputs to the non-columnar mouse V1 from the dorsal lateral geniculate nucleus and feedback projections from multiple higher cortical areas to L1 are patchy. The patches are matched to a pattern of M2 muscarinic acetylcholine receptor expression at fixed locations of mouse, rat and monkey V1. Neurons in L2/3 aligned with M2-rich patches have high spatial acuity whereas cells in M2-poor zones exhibited high temporal acuity. Together M2+ and M2− zones form constant-size domains that are repeated across V1. Domains map subregions of the receptive field, such that multiple copies are contained within the point image. The results suggest that the modular network in mouse V1 selects spatiotemporally distinct clusters of neurons within the point image for top-down control and differential routing of inputs to cortical streams.

INTRODUCTION

In the canonical model, visual perception is a creative process in which the retina transforms luminosity into contrast signals which are sent via the dorsal lateral geniculate nucleus (dLGN) to V1, where they are used to construct receptive fields (RF) selective for features such as oriented edges and stereoscopic depth (Hubel and Wiesel, 1962; Cumming and Parker, 1997). Although many basic features of the natural scene can be perceived though feedforward (FF) processing of visual input (Miller, 2003), disambiguation of complex

images depends on contextual information, attention and prior knowledge (Gilbert and Li, 2013). It is widely held that these influences arise from interactions of FF inputs with horizontal intracortical networks and feedback (FB) inputs from higher cortical areas (Gilbert and Li, 2013). An important node for coupling FF and FB inputs is L1 of V1 (Larkum 2013).

L1 of primate, cat and rodent V1 consists mainly of axon terminals from subcortical sources, as well as from callosal and interareal FB projections synapsing onto apical dendrites of pyramidal cells (PC) whose somata and FF inputs to basal dendrites are in deeper layers (Herkenham, 1980; Felleman and Van Essen, 1991; Binzegger et al. 2004; Rubio-Garrido et al., 2009; Cruikshank et al., 2012; Yang et al., 2013; Cruz-Martinez et al., 2014). PCs in cat and primate V1 are organized in systematic maps of orientation preferences (Blasdel and Salama, 1986; Bonhoeffer and Grinwald, 1991) in which clusters of neurons tuned to similar orientations are connected within a patchy local network (Gilbert and Wiesel, 1989, but see Martin et al., 2014). A similar patchy network provides FB input from V2 to L1 of monkey V1 (Stettler et al., 2002; Angelucci and Bressloff, 2006). But unlike the network within V1, the interareal FB projections lack the like-to-like connectivity (Stettler et al., 2002), suggesting that the patchiness of FB input may be associated with properties of interareal communication rather than with mapping of orientation preferences within V1. This raises the question whether in mouse V1, which lacks orientation columns and is thought to have a random architecture (Ohki and Reid, 2007) L1 contains an orientation-independent map for preferential targeting and selective coupling of inputs to subsets of PCs.

Previous studies in rat V1 have shown that L1 exhibits a fine-scale honeycomb pattern of the vesicular glutamate transporter (VGluT2) expression, interdigitating with zinc-expressing putative intracortical connections and parvalbumin-expressing interneurons (Ichinohe et al., 2003). A similar lattice pattern was observed in rat V1 in the distribution of axon terminals labeled from the dLGN (Rubio-Garrido et al., 2009). Recent observations in mouse V1 have shown that L1 is targeted by matrix-type neurons of the lateral shell of the dLGN, which receive input from direction selective retinal ganglion cells (Cruz-Martinez et al., 2014). Here, we show that in mouse V1 the inputs from the dLGN and higher visual cortical areas are clustered and overlap with a patchy pattern of M2 expression. Further, we found that L2/3 neurons aligned with M2-rich patches have spatiotemporal selectivities that are distinct from neurons in weakly M2-expressing interpatch regions. The results suggest that L1 of mouse V1, which is an important node for associating bottom-up and top-down information, has a non-random architecture that resembles L1 of monkey V1 and may be conserved across mammalian species.

RESULTS

Patchy geniculocortical and intracortical feedback inputs to L1

Studies in rat V1 have shown that expression of VGluT2 in L1 is non-uniform and resembles the honeycomb pattern of geniculocortical input (Ichinohe et al., 2003; Rubio-Garrido et al., 2009). To find out whether geniculocortical projections to L1 of mouse V1 show a similar distribution, we traced axons from the dLGN (N =8) with AAV2/1.pSyn1.EGFP.WPRE.bGH, flattened the cortex and imaged V1 in tangential

sections. We found a striking pattern of periodic densely and weakly innervated patches of axon terminals (Figure 1A). Individual patches were 50–70 μm in diameter with a center-to-center spacing of 100–140 μm. In sharp contrast, the projection to L4 was uniform (not shown). In rat V1, zinc, a modulator of NMDA receptors (Vogt et al., 2000), is expressed in patches of subsets of intracortical terminals (Land and Akhtar, 1999; Ichinohe et al, 2003). To test whether in mouse V1 intracortical FB connections are patchy as well, we traced inputs from extrastriate visual areas, LM (lateromedial, N = 10), AL (anterolateral, N = 6) and RL (rostrolateral, N = 5) (Wang and Burkhalter, 2007). In every case inputs to L1 were patchy. However, the contrast between densely and weakly innervated patches was lower for inputs from LM than for projections from AL (Figure 1D, S1A–C) and RL. We quantified the differences by generating optical density maps of the projections (Figure S2A, B) and comparing axon densities within the densest 30% of patches with the sparsest 30% in the region between neighboring patches. In the projection from LM, the median axon density in the center of patches was about 57% higher than between the patches, suggesting that the projections from a single point are either widespread or the injection site involved neurons of multiple distinct compartments (Figure S2C). Projections from AL and RL showed a bigger (78%) difference ($p<0.05$, ANOVA) between patches and interpatches (Figure S2C), which was comparable to the geniculocortical projection (Figure S2D). The size of corticocortical patches was similar to geniculocortical inputs. In rat V1, VGluT2 and zinc are expressed in complementary sets of terminals (Ichinohe et al., 2003). This raised the question whether geniculocortical and corticocortical inputs were independent of each other. To answer the question we searched for labels with patchy distributions in L1 and L2 similar to the cholinergic markers found in monkey V1 (Horton, 1984; Mrzljak et al., 1996; Tigges et al., 1997). Immunostaining with an antibody against M2 revealed a strikingly non-uniform pattern in L1 (Figure 1B, E). M2-expressing patches tightly overlapped with geniculocortical and intracortical FB projections (Figure 1C, F), suggesting that both of these inputs are not interdigitating as implied by the distributions of VGluT2 and zinc in rat V1 (Ichinohe et al., 2003), but are targeted to fixed, overlapping locations of V1.

Non-random pattern of M2 expression in V1

Next, we were interested in the spatial pattern of M2 expression in V1. In coronal sections, M2 expression was densest in L4, moderate in L1, L3, and L5B, weak in L2 and L6, and barely detectable in L5A (Figure 2A). With the exception of a few isolated nonpyramidal cell bodies, M2 expression was confined to the neuropil. Expression was uniform in all layers except for L1 and L2. Most notably, staining in L1 was clustered in periodic patches of neuropil that were distinct at the L1/2 border, but immediately below the pial surface tended to be fused by bridges of weak M2 expression (Figure 2A). M2 expression in L2 showed a similar periodicity of slender bundles of processes ascending from deeper layers. Staining between vertical M2 bundles in L2 was barely detectable. Counterstaining for Nissl substance showed no matching non-uniformity in cell density. The patchy pattern of M2 expression in L1 and L2 was more readily apparent in tangential sections through flatmounted cortex (Figure 2B). In this plane, V1 had the shape of a shoeprint, which was flanked at the lateral border by a band of retrogradely bisbenzimide labeled callosally-projecting PCs (Wang and Burkhalter, 2007). Although the M2 pattern was patchy and periodic, the lattice order was sometimes obscured by variations in the plane of section and

staining intensity. In sharp contrast, M2 expression in L4 was uniform (Figure 2C). A similar pattern of M2 expression was found in L1 of rat and monkey V1, suggesting that the patchy pattern is conserved across mammalian species (Figure S3, S4). The M2-pattern in monkey V1 showed a peak-to-peak periodicity of ~500 μm and was complementary to cytochrome oxidase (CO)-reactive patches in L1 (Horton, 1984) (Figure S4).

In mouse and rat the patchy M2 expression in superficial layers was also observed in select extrastriate visual areas such as areas LM, LI (intermediolateral), P (posterior) and POR (postrhinal) (Figure 2B; S3). Outside of extrastriate visual cortex, non-uniform M2 expression was found in dorsal retrosplenial cortex (Figure 2B). In contrast, in other parts of extrastriate visual cortex such as areas AL, RL, AM (anteromedial), (PM) posteromedial and MM (mediomedial), M2 expression in L1 and L2 was uniform and weaker. In all extrastriate visual areas M2 expression in L4 was uniform, but the expression density varied in area-specific fashion (Figure 2C).

The patchy M2 immunostaining and the overlap with geniculocortical axon terminals indicated that receptor expression and synaptic inputs to L1 and L2 were preferentially targeted to specific locations while partially sparing others. To determine the periodicity and spatial scale of the patchiness in L1, we generated optical density maps of the tangential distribution of M2 (Figure 3A). The maps revealed a pattern of M2 peaks, whose absolute density varied (depending on plane of section, section thickness and effective staining intensity) across V1, while keeping the ratio between local maxima and minima roughly constant. M2 peaks were readily identified as the center of mass of the densest 30% of the patch. The centroids were used as seed points for dividing V1 into Voronoi polygons, in which each point is closer to its generating center than to all neighboring peaks. Each polygon then represents a domain of graded M2 expression whose density is maximal at the centroid and near minimal along the perimeter. Next, we plotted the spatial density profile of a set of M2 peaks as a function of the distance of each peak from all the others (Rodieck, 1991). Figure 3B shows that the spatial density of M2 peaks in a 1.2×1.2-mm region of the upper central visual field representation in V1 equals the mean of the random distribution, when the distance between centroids exceeds the effective radius of 120 ± 3.6 μm. Notice the prominent repulsion of M2 peaks at distances shorter than 120 μm, indicating that the peaks have a mosaic arrangement with an approximately regular spacing. This raised the question whether M2 peaks are arranged in a square or hexagonal pattern, which is more efficient for image representation (Watson and Ahumada, 1989). To find out we used Gabriel graphing (Gabriel and Sokal, 1969) for identifying neighboring centroids, measured angles between edges connecting neighboring vertices and compared them to angles obtained from seed point patterns generated from square and hexagonal lattice models with varying degrees of jitter. Jitter reflects the offset from the base vertex in proportion to the grid spacing of lattices generated with random origins and rotations (Neyman and Scott, 1958). We found that the probability distribution of the experimentally derived angles was significantly ($P_{K-S}= 5.5*10^{-143}$, Kolmogorov-Smirnov test) different from a nearly perfect square lattice with minimal jitter of 0.1 (Figure 3C). The data also differed significantly ($P_{K-S} < 0.001$) from a square lattice with a jitter of 1 that resembled a lattice drawn from a Poisson distribution (Figure 3C). This analysis supports the result of the density recovery profile (Figure 3B) indicating that the distribution of M2 peaks is non-random. To determine

whether the distribution of M2 peaks was a square or hexagonal lattice, we compared the interneighbor angles with square and hexagonal lattices and variable jitters. A jitter of 0.5, which corresponds to an offset of half the distance between vertices of the normal grid spacing, most closely reproduced the distribution of the measured interneighbor angles. Similar jitter values were found to best reproduce, at a smaller scale, the quasiperiodic daisy architecture of horizontal connections in monkey V1 (Muir et al, 2011). Importantly, the data differed from square ($P_{K-S}= 0.0002$) and hexagonal ($P_{K-S}= 8*10^{-36}$) lattices (Figures 3D, E). Thus, the M2 mosaic most closely resembled ($P_{K-S}= 0.133$) a noisy quasi-rectangular lattice with interneighbor angles of 82°.

Domain size and visual point image

Next we asked whether the sizes of domains and the point image vary across the retinotopic map of V1. We first overlaid the patchy M2 pattern in L1 with the retinotopic coordinates derived by Marshel et al., (2011) and determined the axial lengths of polygons along paths that best matched the azimuth and elevation lines of 10×10 deg tiles at different map locations. We then computed the mean axes of domains within each tile and found that the lengths for azimuth (99–155 μm) and elevation (110–165 μm) varied across V1 (Figure 4A). Notably, however there was no correlation between axial lengths and retinotopic location. In fact, the mean azimuth was remarkably constant (119 ± 4 μm, N = 5) at all elevations across different iso-azimuth bands (Figure 4B) and so was elevation (121 ± 7 μm, N = 5) at all azimuths across different iso-elevation bands (Figure 4C). The results suggest that independent of variations in cortical magnification (Kalatsky and Stryker, 2003; Marshel et al., 2011) V1 is partitioned into constant-size domains centered on M2 peaks.

Next we studied the relationship between domains and the point image in V1. For this purpose we plotted RFs in L2-6 at different locations within the representation of the upper central 60 deg of the visual field, marked the recording sites, immunostained tangential sections for M2 and registered V1 to the retinotopic grid of Marshel et al., (2011) (Figure 5A). The M2 peaks in L1 were used as seed points for tessellation. RFs were assigned to M2+ or M2− zones if they were recorded in the top or bottom 50% of staining density between the nearest neighboring peaks, respectively (Figure 5B). For example in Figure 5B, site 3 was located in M2+ territory, sites 1, 4 and 5 fell into M2− zones, whereas site 2 could not be assigned with confidence to either zone and was discounted.

RFs in L2 and L3 were elliptical (Figure 5C) with shorter ($p < 0.01$, Mann-Whitney U test) axes along elevation than azimuth and similar aspect ratios in M2+ and M2− zones (Figure 6A), supporting an increased magnification along elevation. RFs in L4-6 were more circular with aspect ratios near unity (Figure 6A). The mean RF diameter (determined after transforming an ellipse into a circle of equal area) of L2/3 neurons aligned with M2+ (9.1 ± 0.4 deg) and M2− (10.8 ± 0.3 deg) zones were similar. Neurons recorded on vertical tracks across L2-6 showed overlapping RFs with a mean scatter ([$\Sigma X/Y$ differences of center of N neurons]/N–1]) of 2.6 ± 1.5 deg (Figure 6B), resulting in aggregate RFs that were similar in M2+ (11.7 ± 1.6 deg) and M2− (13.4 ± 1.9 deg) zones.

To compare the amount of cortex taken up by the aggregate RF with the size of a domain, we recorded L2/3 RFs and determined the distance between recording sites that separates

adjoining RFs. Figure 5A–C shows that RF-overlap varied with the distance between recording sites. When recordings were close together (sites 1 and 2, 4 and 5) RFs overlapped. Increasing the distance between sites shifted RFs apart until they represented adjoining parts of the visual field (sites 1 and 5, 2 and 4). The average distance at which this occurred was 361±71 μm (N = 6) for elevation and 247±88 μm (N = 6) for azimuth (Figure 6B). Dividing these distances by the average width of the aggregate RF (12.5 deg), revealed that the approximate magnification factor for elevation is 29 μm/deg and 20 μm/deg for azimuth. Most importantly, the results show that a single domain (Figure 4B, C) is 2–3 times smaller than the block of cortex representing the same point in space, suggesting that multiple domains are contained within the point image (Hubel and Wiesel, 1974).

Non-uniform distribution of domains across V1

As indicated by the triangular shape of V1 (Figures 2B, C, 5A) the block of cortex representing equal degrees of azimuth and elevations is anisotropic (Figure 4A). This raises the questions of how many constant-size domains are contained within a 10×10 deg tile and whether the number varies across the retinotopic map. To find out we overlaid the topographic grid (Marshel et al., 2011) onto the tessellated V1 and determined for each tile how many polygons are optimally aligned along elevation and azimuth. A polygon was considered part of a tile if > 50% of its area was contained within the borders of a tile. Figure 7A shows that 1.7–2.3 polygons were aligned along azimuth and that the number was essentially flat across all iso-elevation bands. By contrast, at most locations of the upper central quadrant, 10 deg of elevation were represented by 3 – 4.5 polygons (Figure 7B). Thus, a 10×10 deg tile in the upper visual field contains 6–10 domains (Figure 7C), suggesting a region of higher domain density similar to a 'central fovea' in V1.

Distinct visual response properties in M2+ and M2− zones

The selective targeting of inputs from the dLGN and extrastriate visual cortex to M2+ patches in L1 raised the question whether L2/3 neurons that are vertically aligned with M2+ and M2− zones have distinct visual response properties. To address this question we recorded single units and characterized responses to drifting gratings of different orientations (OS), contrasts (CS), spatial frequencies (SF) and temporal frequencies (TF). Drifting random dot stimuli were used to determine selectivities to the direction of motion (DS), speed (SS; varying the spatial offset of dots from one video frame to next) and motion coherence (MCS; assessed by varying the proportion of dots moving in the same direction). Random-dot stimuli are broad-band in both SF and TF which scatters the Fourier energy for a drifting dot patch across a sloped line in the joint spatiotemporal frequency domain and indicates that the neuronal response measures true speed tuning (Perrone and Thiele, 2001). Similarly the power spectrum of low coherence stimuli is lower than that to high coherence stimuli, indicating that coherence measures tuning to the strength of motion (Britten et al., 1992). Recording sites were marked with DiI and assigned using optical density maps of M2-stained tangential sections to M2+ and M2− zones (Figure S5). In both zones, many neurons were tuned ($p < 0.05$, ANOVA) selectively (DI $\geq$ 0.425, corresponding to a 2:1 difference between maximal and minimal response) for OS, DS, SS, MCS, CS, SF and TF. Most interestingly, the properties were preferentially distributed in M2+ and M2− zones. For example, the cell recorded in the M2+ zone showed sharp OS, broad DS, preferred slow

speeds, was not tuned to MCS, showed moderately high CS, and preferred high SF and low TF (Figure S6A–G). In contrast, the cell in the M2− zone showed no OS, sharp DS, preferred high speeds, was MCS tuned, showed moderate CS, and preferred low SF and high TF (Figure S6A–G). The zone-specific distribution of selectivities and tuning strengths was confirmed by population data. OS neurons were 2.5-fold ($p < 0.01$, Chi-square) more frequent and more robustly tuned ($p < 0.01$, Mann-Whitney U test) in M2+ than M2− zones (Figure 8A, S7A). In contrast, DS neurons in M2− zones were twice as numerous ($p < 0.05$, Chi-square) and more strongly tuned ($p < 0.01$, Mann-Whitney U test) than in M2+ zones (Figure 8A, S7B). Similarly, M2− zones contained twice as many ($p < 0.01$, Chi-square) SS neurons, which were more sharply ($p < 0.05$, Mann-Whitney U test) tuned and responsive to peak speeds double those found in M2+ zones ($p < 0.05$, Mann-Whitney) (Figure 8A, S7C, D). Likewise, motion coherence tuned neurons were almost 3-fold more frequent ($p < 0.01$, Chi-square) and more strongly ($p < 0.01$, Mann-Whitney U test) tuned in M2− than M2+ zones (Figure 8A, S7E). Almost all neurons in M2+ and M2− zones were CS and exhibited similar tuning strengths and C50 (Figure 8A, S7F, G). The vast majority of neurons in M2+ and M2− zones were SF and TF and showed similar tuning strengths (Figure 8A, S7H, I). However, low-pass TF tuning was more frequent in M2+ zones (77%), whereas band-pass tuning was more common (75%) in M2− zones (Figure 8A).

While the overall percentage and tuning strength for SF and TF was identical in both zones, cells aligned with M2+ and M2− zones showed distinct spatiotemporal sensitivities. Neurons in M2+ zones preferred significantly ($p < 0.01$, Mann-Whitney U test) higher SF (0.052 c/deg), median half bandwidth at half maximal height) than cells in M2− zones (0.021 c/deg) (Figure 8B). The opposite distribution was observed for TF, where the median peak sensitivity in M2− zones (1.83 Hz) was significantly ($p < 0.01$, Mann-Whitney U test) higher than in M2+ zones (1.27 Hz) (Figure 8E). Consistent with the zone-specific distribution of SF and TF, neurons in M2− zones showed significantly ($p < 0.05$, Mann-Whitney U test) higher median peak speeds (21 deg/s) than cells in M2+ zones (9.5 deg/s) (Figure S7D). The zone-specific differences in SF and TF sensitivities were also observed in subsets of OS and DS neurons (Figures 8C, D, F, G), indicating that the diverse spatiotemporal sensitivities are not tied to specific feature selectivities, rather that they are linked to the cells' locations in M2+ and M2− zones.

To further test the contrasting SF and TF tuning in M2+ and M2− zones, we analyzed stimulus sensitivities on a cell-by-cell basis. Notably, cells in M2+ zones were sensitive over a broad range of SFs and a narrow range of TFs (Figure 8H). In contrast, M2− cells were sensitive to a broad window of TFs and a narrow range of SFs (Figure 8H). The differences of SF and TF preferences in M2+ and M2− zones were significant ($p < 0.01$, Mann Whitney U test), suggesting that the spatiotemporal sensitivities of individual neurons in M2+ and M2− zones are distinct.

DISCUSSION

We have found that L1 of the non-columnar mouse V1 (Ohki and Reid, 2007) is modularly organized. The modularity is expressed by clustered inputs from the dLGN as well as FB inputs from higher visual areas, converging onto a quasi-rectangular pattern of M2-

immunostained patches in L1. The patches are small (~ 60 μm) and narrowly spaced apart (~120 μm) so that multiple copies fit into the cortical point image. Although the M2 matrix is largely confined to L1, it provides scaffolding for clusters of L2/3 PCs with distinct spatiotemporal selectivities: cells aligned with M2+ zones prefer high SF and low TF whereas cells associated with M2− zones favor low SF and high TF. The modularity suggests that apical dendrites in L1 of PCs tuned to high SF and low TF are preferentially targeted by convergent dLGN and FB inputs from areas of the dorsal and ventral streams (Wang et al, 2012). Thus, it is conceivable that coincident FB input to L1 and FF input to basal dendrites in deep L2/3 modulate the output of a subclass of PCs in stream-dependent fashion.

Multiple modules contained in point image

Previous studies in rat V1 have shown an interdigitating expression of VGluT2 and zinc in terminal patches of L1 with a center-to center spacing comparable to the patterns observed in mouse V1 (Ichinohe et al., 2003). VGluT2 is a putative marker of geniculocortical input (Fujiyama et al., 2001), which was shown to terminate in patchy fashion in L1 of rat and mouse V1 (Rubio-Garrido et al., 2009; this study). Using the dLGN input as reference it is likely that VGluT2-expressing patches in rat correspond to M2+ zones in mouse. This interpretation is consistent with observations that M2 expression in L1 is down-regulated by genetic deletion of the geniculocortical pathway (Chou et al., 2013). We found that inputs from the dLGN and the higher visual areas, LM, AL and RL, preferentially terminate in M2+ zones and tend to avoid M2− zones. This contrasts with the preferential targeting of zinc-expressing putative corticocortical input to VGluT2-negative patches in rat V1 (Ichinohe et al., 2003). However, the results in rat suggest that zinc might be more widely distributed in mouse V1 and that M2− patches most likely receive input from areas other than LM, AL and RL. Although we have focused on V1, it is important to note that M2-expressing L1 modules also exist in visual areas of the ventral stream (LM, LI, P, POR) as well as in retrosplenial cortex (RS). Similar to V1, patches in RS express a cholinergic marker (acetylcholinesterase) and receive input from the thalamus (Wyss et al., 1990). Thus, partitioning L1 into topologically fixed, constant-size domains is a widely used motif in rodent cortex.

We found that individual domains represent only a small portion of a RF, indicating that multiple domains are contained within the 361 μm (elevation) × 247 μm (azimuth)-wide point image covering ~9 × 15 deg of visual space. The anisotropy matched that of individual RFs in L2/3 and accounts for the axial difference of cortical magnification. Within the point image the retinotopy was course, as reported previously (Smith and Häusser, 2010; Bonin et al., 2011). Notably, higher cortical magnification is achieved by increasing the number of domains rather by making them larger. This design is evident by increasing the density of domains in the upper visual field representation of V1, which receives preferential input from local edge detecting retinal ganglion cells (Zhang et al., 2012; Bleckert et al., 2014) and are thought to play a role in the recognition of predators (Wallace et al., 2013). The presence of multiple domains within the point image resonates with the multi-blob architecture of hypercolumns in primate V1 (Livingstone and Hubel, 1984). The stereotyped modularity of V1 across species suggests that neurons aligned with M2+ and M2− zones

may be clonally related and that the ~30–60 μm-wide radial columns observed in developing mouse cortex are linked to the periodicity observed here (Torii et al., 2009).

Modular organization of connections

We found that the *clustered* geniculocortical and intracortical FB connections to V1 are largely confined to L1. Unlike L2–6 which receives most of its inputs from neighboring neurons, most inputs to L1 originate from extrinsic sources (Binzegger et al., 2004), such as the brain stem, basal forebrain, thalamus, contralateral cortex and ipsilateral higher cortical areas (Herkenham, 1980; Morrison et al., 1982; Cruickshank et al., 2012; Alito et al., 2013; Yang et al., 2013; Cruz-Martinez et al., 2014). Of these, inputs originating from matrix-type dLGN neurons were shown to be patchy in rat V1 (Rubio-Garrido et al., 2009). Clustered FB projections were observed previously between monkey V2 and V1 (Stettler et al., 2002; Angelucci and Bressloff, 2006). Importantly, the patchiness in monkey did not show the like-to-like connectivity known for columns with similar orientation preferences, suggesting that clustering of FB input to L1 is unrelated to the systematic mapping of orientation in V1 (Stettler et al., 2002). The independence of the patchy connectivity from the orderly map of orientation, which is absent in mice (Ohki and Reid, 2007), further suggests that the pattern is not directly related to the intrinsic network of V1. Rather, it represents an evolutionarily conserved network for distributed processing across multiple functionally specialized areas.

We found that the clustered geniculocortical and intracortical inputs to L1 overlap with a fixed matrix of M2-expressing patches. In cat and monkey both of these inputs terminate at dendritic spines of PCs (Anderson et al., 1992; Anderson et al., 2011). Recordings in mouse barrel, motor and visual cortex have shown that matrix-type thalamocortical and intracortical FB inputs to L1 synaptically activate dendrites of L2/3 and 5 PCs (Petreanu et al., 2009; Hooks et al., 2013; Yang et al., 2013). Our data imply that such inputs to M2+ zones are stronger than to M2− zones and may drive different subtypes of PCs. This notion is supported by putative thalamocortical inputs to M2+ zones (this study) presumably synapsing on thick dendrites of microtubule-associated protein 2 (MAP2)-expressing L2/3 and 5 PCs (Ichinohe et al., 2003). In contrast, input to M2− zones may contact thinner dendrites, which co-localize MAP2 and the olfactory cell adhesion molecule (OCAM) (Ichinohe et al., 2003; Ichinohe et al., 2008). Thus, PCs with apical dendrites in M2+ zones may receive inputs from matrix-type thalamocortical neurons and L5 PCs, whereas cells with dendrites in M2− zones may receive core-type thalamocortical input (Feldmeyer, 2012; Harris and Shepherd, 2015). This mosaic organization is consistent with the minicolumnar array of PCs, projecting to diverse intracortical and subcortical targets (Innocenti and Vercelli, 2010). In addition, the organization fits with observations that V1 neurons with different responses preferences provide input to distinct visual areas (Matsui and Ohki, 2013; Glickfeld et al., 2013).

A major finding of our study is that inputs from the dLGN and higher visual areas converge onto M2+ zones in V1. In a distributed cortical network, an important task of PCs is to associate FB input entering at distal dendrites with coincident core-type thalamocortical input from basal dendrites (Larkum, 2013). The mechanism by which this might be achieved is through spikes triggered by inputs to basal dendrites backpropagating into apical dendrites

and influencing spike output by coincident synaptic input to L1 (Larkum et al., 1999; Shai et al., 2015). The integration of dendritic depolarizations from diverse sources is known to affect the strength and selectivity of PC output (Xu et al., 2012; Smith et al., 2013; Palmer et al., 2014). The patchy connectivity we have found suggests that this process is more common in L2/3 and L5 PCs aligned with M2+ than M2− patches (Larkum et al., 2007). Thus, the overlap of inputs from matrix-type dLGN, LM, AL and RL in L1 may play a role in influencing responses in subsets of PCs by top down inputs from 'where' and 'what' streams in task-specific fashion (Chen et al., 2013; Yamashita et al., 2013). This process may be modulated by activating M2 receptors, decorrelating visual responses and drive neurons to carry independent information (Vinje and Gallant, 2000; Goard and Dan, 2009).

Clustering neurons into spatiotemporal frequency domains

We found that superficial layer V1 neurons aligned with M2+ and M2− zones in L1 have distinct spatiotemporal response properties and that multiple distinct clusters are contained within the point image. This heterogeneity is reminiscent of the distribution of ON and OFF subregions within a RF (Smith and Häusser, 2010; Bonin et al., 2011). The diverse groups of V1 neurons we have found resemble the two classes of dLGN neurons with either canonical center-surround properties including sensitivities to low SF/high TF/high SS or non-canonical tuning with sensitivities to high SF/low TF/low SS (Piscopo et al., 2013). The similarity of functional groups in dLGN and V1 suggests that input from non-canonical neurons targets M2+ patches, whereas cells aligned with M2− patches receive input from canonical-type dLGN neurons. The spatial grouping of neurons in mouse V1 is consistent with the pattern of two sets of domains in monkey and cat striate cortex for low SF in CO-rich blobs and high SF in CO-poor interblobs, respectively (Tootell et al., 1988; Born and Tootell, 1991; Hübener et al., 1997). Moreover, similar to mouse V1 the high SF interblob compartment in primate V1 expresses M2 in PCs and interneurons at pre- and postsynaptic asymmetric and symmetric contacts (Mrzljak et al., 1996; Tigges et al., 1997; Zeisel et al., 2015; this study). Thus, it appears that the patchy pattern of M2 expression segregates neurons with conflicting requirements for high spatial- and high temporal resolution vision (Schiller and Logothetis, 1990). The presence of multiple modules in the point image superimposed onto the random distribution of orientation preferences (Ohki and Reid, 2007) ensures the complete coverage by all possible stimulus selectivities within a region of cortex dedicated to the analysis of inputs from the same point in space.

EXPERIMETAL PROCEDURES

Tracing connections, immunocytochemistry and image analysis

All experimental procedures were approved by the Washington University's Animal Care and Use Committee. Five to eight week-old male and female C57BL/6J, C57BL/6-M2−/− mice and 4 month-old male Long-Evans rats were anesthetized with ketamine/xylazine (86 mg·kg^{-1}/13 mg·kg^{-1}, i.p.). The visual cortex of a 9-year old male rhesus monkey, involved in a terminal study unrelated to the present investigation was obtained (gift from Lawrence Tychsen, Washington University), after euthanasia (150 mg/kg pentobarbital) and perfusion with phosphate buffered 4% paraformaldehyde.

In mice, connections to V1 from the dLGN and extrastriate visual areas LM, AL and RL were labeled anterogradely by pressure injection of AAV2/1.pSyn1.EGFP.WPRE.bGH. Callosal connections were traced retrogradely by pressure injection of bisbenzimide. Postsurgical survival times were 4 days for bisbenzimide and 21 days for the virus. Rodents were euthanized and perfused with paraformaldehyde. The cortex of rodents was either cut in the transverse plane or flatmounted and cut tangentially at 40 μm. Monkey V1 was flatmounted and sectioned tangentially. Sections from mice, rats and monkey were incubated with an antibody against the M2 muscarinic acetylcholine receptor, which was visualized with an Alexa Fluor 647-labled secondary antibody. Immunostained monkey sections were in addition stained for CO activity. M2–, CO– and axonal projection patterns were imaged under a microscope equipped with fluorescence and bright field optics. Images of patchy tangential labeling patterns in V1 were converted to optical-density maps. The distribution of M2 patches was extracted from centroids of the densest 30% of local peaks, which were used as seed points for Voronoi tessellation. Voronoi polygons demarcated domains of graded M2 expression. Axial lengths (azimuth, elevation), number and distribution of polygons across V1 were determined by aligning the retinotopic grid by Marshel et al., (2011) and measuring the distances between centroids and interneighbor angles.

Visual stimulation and single unit recordings—Drifting sinusoidal gratings were used for examining OS, CS, SF, TF tuning whereas DS, SS and MCS was measured with drifting random dot patterns displayed on a monitor at 22.5 cm viewing distance centered on the right eye at different locations of the visual field. Mice were anesthetized with urethane (20%, 0.2ml/20 g body weight, IP). Recordings were made with tungsten electrodes at different locations of V1. Recording sites in V1 were marked by DiI deposits, whose locations within domains were identified after staining tangential sections with an antibody against M2. Neural signals were filtered; single units were isolated and stored in a computer. RF size was determined quantitatively from spatial plots outlining the contour corresponding to 2 SDs of the response. The overlap between neighboring RFs was computed as the absolute value of the difference of the distance between RF centers and the sum of the RF radii. ANOVA was used to assess significant ($p < 0.05$) tuning. Tuning curves were fit with functions that best described the data with the smallest number of parameters (Gao et al., 2010). Selective tuning was assessed by a discrimination index. See Supplemental Experimental Procedures for more details and statistics.

Supplementary Material

Refer to Web version on PubMed Central for supplementary material.

Acknowledgments

References

Alito HJ, Dan Y. Cell-type-specific modulation of neocortical activity by basal forebrain input. Front Syst Neurosci. 2013; 6:1–12.

Anderson JC, Dehay C, Friedlander MJ, Martin KAC, Nelson JC. Synaptic connections of physiologically identified geniculocortical axons in kitten cortical area 17. Proc R Soc Lond B. 1992; 250:187–194.

Anderson JC, Kennedy H, Martin KAC. Pathways of attention: synaptic relationships of frontal eye field to V4, lateral intraparietal cortex, and area 46 in macaque monkey. J Neurosci. 2011; 31:10872–10881. [PubMed: 21795539]

Angelucci A, Bressloff PC. Contribution of feedforward, lateral and feedback connections to the classical receptive field center and extra-classical receptive field surround of primate V1 neurons. Prog Brain Res. 2006; 154:93–120. [PubMed: 17010705]

Binzegger T, Douglas RJ, Martin KAC. A quantitative map of the circuit of cat primary visual cortex. J Neurosci. 2004; 24:8441–8453. [PubMed: 15456817]

Blasdel GG, Salama G. Voltage-sensitive dyes reveal a modular organization in monkey striate cortex. Nature. 1986; 321:579–585. [PubMed: 3713842]

Bleckert A, Schwartz GW, Turner MH, Rieke F, Wong ROL. Visual space is represented by nonmatching topographies of distinct mouse retinal ganglion cell types. Curr Biol. 2014; 24:310–315. [PubMed: 24440397]

Bonhoeffer T, Grinvald A. Iso-orientation domains in cat visual cortex are arranged in pinwheel-like patterns. Nature. 1991; 353:429–431. [PubMed: 1896085]

Bonin V, Histed MH, Yurgenson S, Reid RC. Local diversity and fine-scale organization of receptive fields in mice visual cortex. J Neurosci. 2011; 31:18506–18521. [PubMed: 22171051]

Born RT, Tootell RBH. Spatial frequency tuning of single units in macaque supragranular striate cortex. Proc Natl Acad Sci USA. 1991; 88:7066–7070. [PubMed: 1651492]

Britten KH, Shadlen MN, Newson WT, Movshon AJ. Responses of neurons in macaque MT to stochastic motion signals. Vis Neurosci. 1992; 10:1157–1169. [PubMed: 8257671]

Chen JL, Carta S, Soldano-Magraner J, Schneider BL, Helmchen F. Behaviour-dependent recruitment of long-range projection neurons in somatosensory cortex. Nature. 2013; 499:336–340. [PubMed: 23792559]

Chou SJ, Babot Z, Leingärtner A, Studer M, Nakagawa Y, O'Leary DDM. Geniculocortical input drives genetic distinctions between primary and higher-order visual areas. Science. 2013; 340:1239–1242. [PubMed: 23744949]

Cruikshank SJ, Ahmed OJ, Stevens TR, Patrick SL, Gonzale AN, Elmaleh M, Connors BW. Thalamic control of layer 1 circuits in prefrontal cortex. J Neurosci. 2012; 32:17813–17823. [PubMed: 23223300]

Cumming BG, Parker AJ. Responses of primary visual cortical neurons to binocular disparity without depth perception. Nature. 1997; 389:280–283. [PubMed: 9305841]

Cruz-Martinez A, El-Danaf RN, Osakada F, Sriram B, Dhande OS, Nguyen PL, Callaway EM, Gosh A, Huberman AD. A dedicated circuit links direction-selective retinal ganglion cells to the primary visual cortex. Nature. 2014; 507:358–361. [PubMed: 24572358]

Feldmeyer D. Excitatory neuronal connectivity in the barrel cortex. Front Neuroant. 2012; 6:1–22.

Felleman DJ, Van Essen DC. Distributed hierarchical processing in the primate cerebral cortex. Cereb Cortex. 1991; 1:1–47. [PubMed: 1822724]

Fujiyama F, Furuta T, Kaneko Y. Immunocytochemical localization of candidates for vesicular glutamate transporters in the rat cerebral cortex. J Comp Neurol. 2001; 435:379–387. [PubMed: 11406819]

Gabriel KR, Sokal RR. A new statistical approach to geographic variation analysis. Syst Zool. 1969; 18:258–278.

Gao E, DeAngelis GC, Burkhalter A. Parallel input channels to mouse primary visual cortex. J Neurosci. 2010; 30:5912–5926. [PubMed: 20427651]

Author Manuscript

Author Manuscript

Author Manuscript

Author Manuscript

Gilbert CD, Wiesel TN. Columnar specificity of intrinsic horizontal and corticocortical connections in cat visual cortex. J Neurosci. 1989; 9:2432–2442. [PubMed: 2746337]

Gilbert CD, Li W. Top-down influences on visual processing. Nat Rev Neurosci. 2013; 14:350–363. [PubMed: 23595013]

Glickfeld LL, Andermann ML, Bonin V, Reid RC. Cortico-cortical projections in mouse visual cortex are functionally target specific. Nat Neurosci. 2013; 16:219226.

Goard M, Dan Y. Basal forebrain activation enhances cortical coding of natural scenes. Nat Neurosci. 2009; 11:14401445.

Harris KD, Shepherd GMG. The neocortical circuit themes and variations. Nat Neurosci. 2015; 18:170–181. [PubMed: 25622573]

Herkenham M. Laminar organization of thalamic projections in the rat neocortex. Science. 1980; 207:532–535. [PubMed: 7352263]

Hooks BM, Mao T, Gutinsky DA, Yamawaki N, Svoboda K, Shepherd GM. Organization of cortical and thalamic input to pyramidal neuron sin mouse motor cortex. J Neurosci. 2013; 33:748–760. [PubMed: 23303952]

Horton JC. Cytochrome oxidase patches: a new cytoarchitectonic feature of monkey visual cortex. Phil Trans R Soc Lond B. 1984; 304:199–253. [PubMed: 6142484]

Hubel DH, Wiesel TN. Receptive fields, binocular interaction and functional architecture in the cat's visual cortex. J Physiol. 1962; 160:106–154. [PubMed: 14449617]

Hubel DH, Wiesel TN. Uniformity of monkey striate cortex: a parallel relationship between field size, scatter, and magnification factor. J Comp Neurol. 1974; 158:295–305. [PubMed: 4436457]

Hübener M, Shoham D, Grinvald A, Bonhoeffer T. Spatial relationships among three columnar systems in cat area 17. J Neurosci. 1997; 17:9270–9284. [PubMed: 9364073]

Ichinohe N, Fujiyama F, Kaneko T, Rockland KS. Honeycomb-like mosaic at the border of layers 1 and 2 in the cerebral cortex. J Neurosci. 2003; 23:1372–1382.

Ichinohe N, Knight A, Ogawa M, Ohshima T, Mikoshiba K, Yoshihara Y, Terashima T, Rockland KS. Unusual patch-matrix organization in the retrosplenial cortex of the reeler mouse and shaking rat Kawasaki. Cereb Cortex. 2008; 18:1125–1138. [PubMed: 17728262]

Innocenti GM, Vercelli A. Dendritic bundles, minicolumns, columns, and cortical output units. Front Neuroanat. 2010; 4:1–7. [PubMed: 20161990]

Kalatsky VA, Stryker MP. New paradigm for optical imaging: temporally encoded maps for intrinsic signal. Neuron. 2003; 38:529–545. [PubMed: 12765606]

Land PW, Akhtar ND. Experience-dependent alteration of synaptic zinc in rat somatosensory barrel cortex. Somtaosens Mot Res. 1999; 16:139–150.

Larkum M. A cellular mechanism for cortical associations: an organizing principle for the cerebral cortex. Trends Neurosci. 2013; 36:141–151. [PubMed: 23273272]

Larkum ME, Zhu JJ, Sakmann B. A new cellular mechanism for coupling inputs arriving at different cortical layers. Nature. 1999; 398:338–341. [PubMed: 10192334]

Larkum ME, Waters J, Sakmann B, Helmchen F. Dendritic spikes in apical dendrites of neocortical layer 2/3 pyramidal neurons. J Neurosci. 2007; 27:8999–9008. [PubMed: 17715337]

Livingstone MS, Hubel DH. Anatomy and physiology of a color system in the primate visual cortex. J Neurosci. 1984; 4:309–356. [PubMed: 6198495]

Marshel JH, Garrett ME, Nauhaus I, Callaway EM. Functional specialization of seven mouse visual cortical areas. Neuron. 2011; 72:1040–1054. [PubMed: 22196338]

Martin KAC, Roth S, Rusch ES. Superficial layer pyramidal cells communicate heterogeneously between multiple functional domains of cat primary visual cortex. Nat Communication. 2014; 5:1–13.

Matsui Y, Ohki K. Target dependence of orientation and direction selectivity of corticocortical projection neurons in the mouse V1. Front Neur Circuits. 2013; 7:1–9.

Miller KD. Understanding layer 4 of the cortical circuit: a model based on cat V1. Cereb Cortex. 2003; 13:73–82. [PubMed: 12466218]

Morrison JH, Foote SL, Molliver ME, Bloom FE, Lidov HGW. Noradrenergic and serotonergic fibers innervate complementary layers in monkey primary visual cortex: an immunohistochemical study. Proc Natl Acad Sci USA. 1982; 79:2401–2405. [PubMed: 7048320]

Muir DR, Da Costa NM, Girardin CC, Naaman S, Omer DB, Ruesch E, Grinvald A, Douglas DJ. Embedding of cortical representations by the superficial patch system. Cerebral Cortex. 2011; 21:2244–2260. [PubMed: 21383233]

Mrzljak L, Levey AI, Goldman-Rakic PS. Selective expression of m2 muscarinic receptor in the parvocellular channel of the primate visual cortex. Proc Natl Acad Sci USA. 1996; 93:7337–7340. [PubMed: 8692994]

Neyman J, Scott EL. Statistical approach to problems of cosmology. J R Stat Soc B. 1958; 21:1–43.

Ohki K, Reid RC. Specificity and randomness in the visual cortex. Curr Opin Neurobiol. 2007; 17:401–407. [PubMed: 17720489]

Palmer LM, Shai AS, Reeve JE, Anderson HL, Paulsen O, Larkum ME. NMDA spikes enhance action potential generation during sensory input. Nat Neurosci. 2014; 17:383–390. [PubMed: 24487231]

Perrone JA, Thiele A. Speed skills: measuring the visual speed analyzing properties of primate MT neurons. Nat Neurosci. 2001; 4:526–532. [PubMed: 11319562]

Petreanu L, Mao T, Sternson SM, Svoboda K. The subcellular organization of neocortical excitatory connections. Nature. 2009; 457:112–1150.

Piscopo DM, El-Danaf RN, Huberman AD, Niell CM. Diverse visual features encoded in mouse lateral geniculate nucleus. J Neurosci. 2013; 33:4642–4656. [PubMed: 23486939]

Rodieck RW. The density recovery profile: A method for the analysis of points in the plane applicable to retinal studies. Vis Neurosci. 1991; 6:95–111. [PubMed: 2049333]

Rubio-Garrido P, Pérez-de-Manzo F, Porrero C, Galazo MJ, Clascà F. Thalamic input to distal apical dendrites in neocortical layer 1 is massive and highly convergent. Cereb Cortex. 2009; 19:2380–2395. [PubMed: 19188274]

Schiller PH, Logothetis NK. The color-opponent and broad-band channels of the primate visual system. Trends Neurosci. 1990; 13:392–398. [PubMed: 1700509]

Shai AS, Anastassiou CA, Larkum ME, Koch C. Physiology of layer 5 pyramidal neuron in mouse primary visual cortex: Coincidence detection through bursting. PLOS Comp Biol. 2015; 11:1–18.

Smith SL, Häusser M. Parallel processing of visual space by neighboring neurons in mouse visual cortex. Nat Neurosci. 2010; 13:1144–1149. [PubMed: 20711183]

Smith SL, Smith IT, Branco T, Häusser M. Dendritic spikes enhance stimulus selectivity in cortical neurons in vivo. Nature. 2013; 503:115–120. [PubMed: 24162850]

Stettler DD, Das A, Bennett J, Gilbert CD. Lateral connectivity and contextual interactions in macaque primary visual cortex. Neuron. 2002; 36:739–750. [PubMed: 12441061]

Tigges M, Tigges J, Rees H, Rye D, Levey A. Distribution of muscarinic cholinergic receptor proteins m1 to m4 in area 17 of normal and monocularly deprived rhesus monkeys. J Comp Neurol. 1997; 388:130–145. [PubMed: 9364243]

Torii M, Hashimoto-Torii K, Levitt P, Rakic P. Integration of neuronal clones in the radial cortical columns by EphA/ephrin-A signaling. Nature. 2009; 461:524–528. [PubMed: 19759535]

Tootell RBH, Silverman MS, Hamilton SL, Switkes E, De Valois RL. Functional anatomy of macaque striate cortex. V. Spatial frequency. J Neurosci. 1988; 8:1610–1623. [PubMed: 3367213]

Vinje WE, Gallant JL. Sparse coding and decorrelation in primary visual cortex during natural vision. Science. 2000; 287:1273–1276. [PubMed: 10678835]

Vogt K, Mellor J, Tong G, Nicoll RA. The actions of synaptically released zinc at hippocampal mossy fiber synapses. Neuron. 2000; 26:187–196. [PubMed: 10798403]

Wallace DJ, Greenberg DS, Sawinski J, Rulla S, Notaro G, Kerr JND. Rats maintain an overhead binocular field at the expense of constant fusion. Nature. 2013; 498:65–69. [PubMed: 23708965]

Wang Q, Burkhalter A. Area map of mouse visual cortex. J Comp Neurol. 2007; 502:339–357. [PubMed: 17366604]

Wang Q, Sporns O, Burkhalter A. Network analysis of corticocortical connections reveals ventral and dorsal processing streams in mouse visual cortex. J Neurosci. 2012; 32:4386–4399. [PubMed: 22457489]

Watson AB, Ahumada AJ Jr. A hexagonal orthogonal-orientated pyramid as model of image representation in visual cortex. IEEE Trans Biomed Engineering. 1989; 36:97–106.

Wyss MJ, Van Goen T, Sripanidkulchai K. Dendritic bundling in layer 1 of granular retrosplenial cortex: intracellular labeling and selectivity of innervation. J Comp Neurol. 1990; 295:33–42. [PubMed: 2341634]

Xu NL, Harnett MT, Williams SR, Huber D, O'Connor DH, Svoboda K, Magee JC. Nonlinear dendritic integration of sensory and motor input during active sensing. Nature. 2012; 492:247–251. [PubMed: 23143335]

Yamashita T, Pala A, Pedrido L, Kremer Y, Welker E, Petersen CCH. Membrane potential dynamics of neocortical projection neurons driving target-specific signals. Neuron. 2013; 80:1477–1490. [PubMed: 24360548]

Yang W, Carrasquillo Y, Hooks BM, Nerbonne JM, Burkhalter A. Distinct balance of excitation and inhibition in an interareal feedforward and feedback circuit of mouse visual cortex. J Neurosci. 2013; 33:17373–17384. [PubMed: 24174670]

Zeisel A, Muñoz-Manchado AB, Codeluppi S, Lönnerberg P, La Manno G, Juréus A, Marques S, Munguba H, He L, Betsholtz C, Rolny C, Castelo-Branco G, Hjerling-Leffer J, Linnarsson S. Cell types In the mouse cortex and hippocampus revealed by single-cell RNA-seq. Science. 2015; 347:11381142.

Zhang Y, Kim IJ, Sanes JR, Meister M. The most numerous ganglion cell types of the mouse retina is a selective feature detector. Proc Natl Acad Sci USA. 2012; 109:E2391–E2398. [PubMed: 22891316]

Highlights

- Patchy organization of geniculocortical and intracortical input to layer 1of V1

- Patchy inputs to layer 1 overlap with patchy expression of M2 acetylcholine receptor

- Distinct spatiotemporal sensitivities of neurons aligned with patches in layer 1

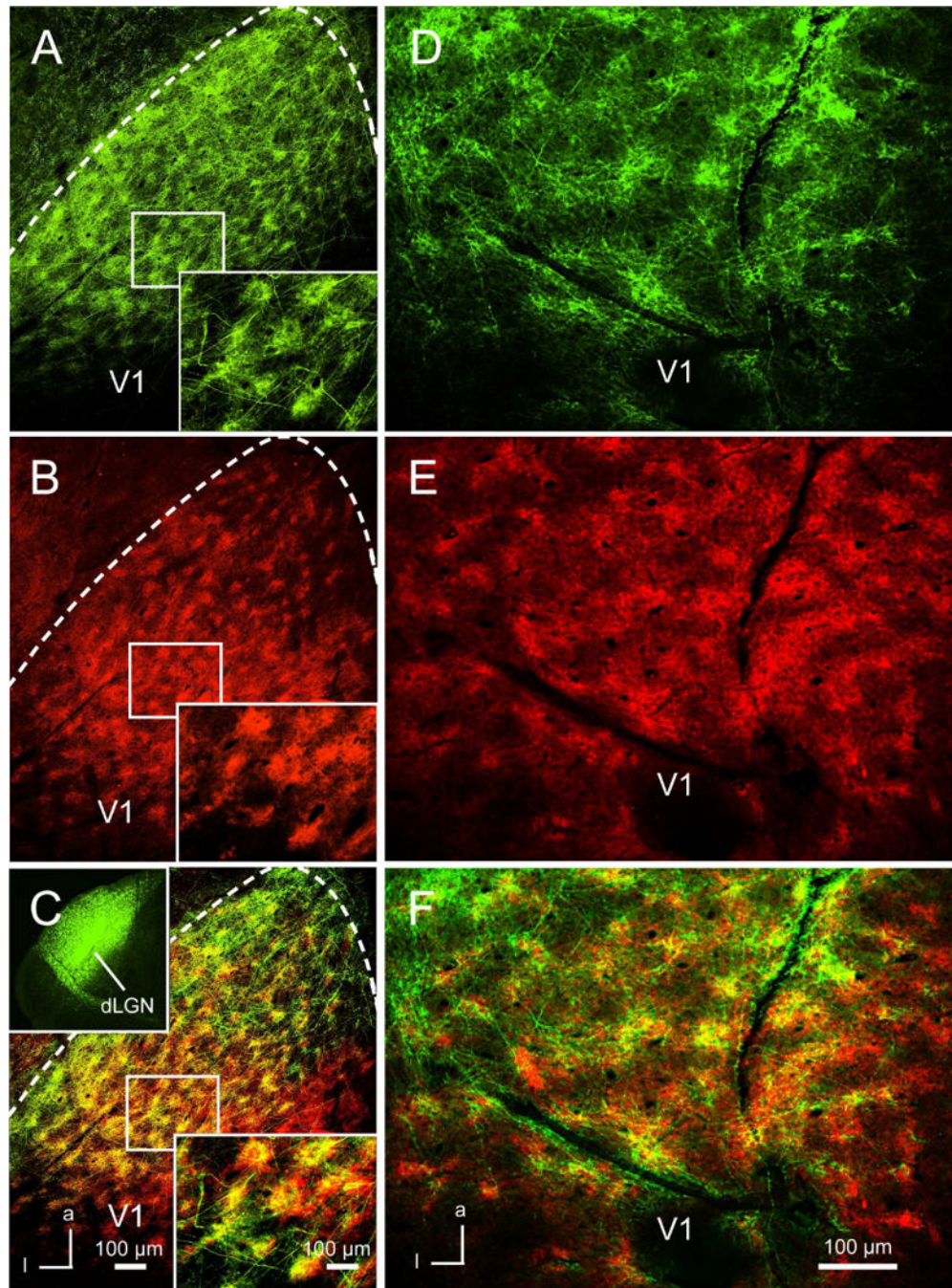- Multiple patches contained within point image

Figure 1. Overlapping patchy patterns of geniculocortical and intracortical feedback projections with M2-expressing patches in L1 of mouse V1

(A) Tangential section through L1 of V1 showing patchy pattern of geniculocortical projections labeled by axonal tracing with AAV2/1.pSyn1.EGFP.WPRE.bGH from the dLGN (inset in C). (B) Section illustrated in (A) stained with an antibody against M2 showing patchy expression of M2. (C) Overlay of (A) and (B), showing overlap (yellow) of geniculocortical projections and M2 patches in V1. Boxed area shows magnification. (D) Tangential section through L1 of V1, showing AAV2/1.pSyn1.EGFP.WPRE.bGH labeled projections from area AL (for injection site see Figure S1). (E) Section shown in (D)

immunolabled for M2. (F) Overlay of (D) and (E) showing overlap of FB projections and M2 patches in V1. Anterior (a), Lateral (l).
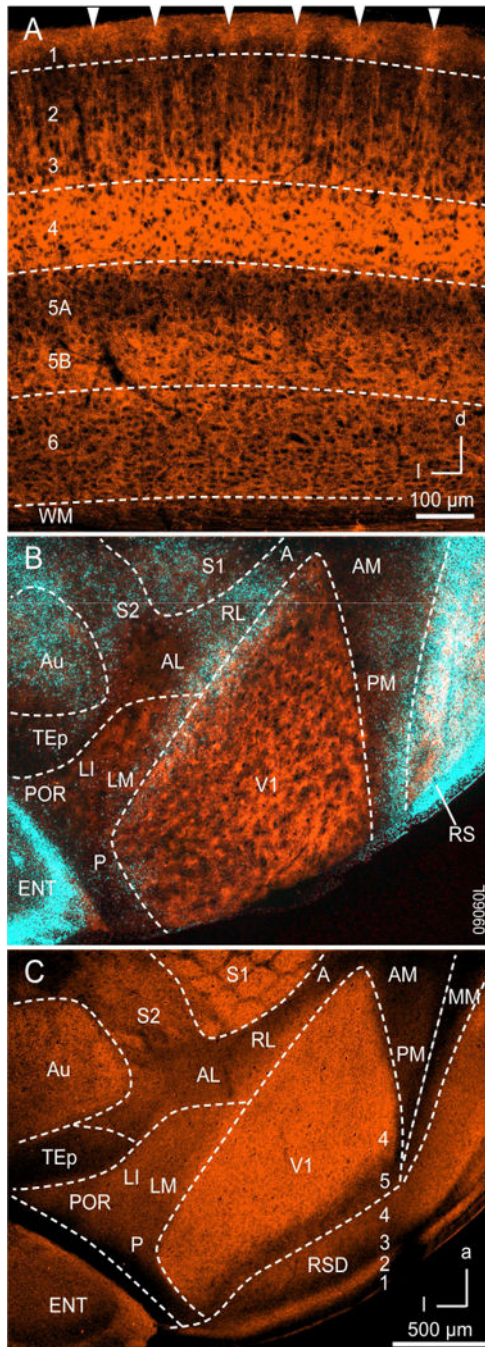
Figure 2. Expression of M2 muscarinic acetylcholine receptors in mouse visual cortex
(A) Coronal section through V1 stained with antibody against M2. M2 expression is strongest in L4 and L3, moderate in L1, L2, L5B, sparse in L6 and barely detectable in L5A. M2 expression is uniform in L4-6, but patchy in L1 (arrowheads) and shows periodic, slender vertical bands in L2. Lateral (L), dorsal (D). (B) M2 immunostained tangential section through L1 of occipital cortex. M2 expression (red) in V1 is non-uniform and patchy. The patchy pattern is also observed in a region of extrastriate visual cortex which includes areas LM, LI, P and POR. M2 expression in areas AL, RL, A, AM and P is weak

and uniform. Blue staining represents retrogradely bisbenzimide labeled callosally-projecting neurons, used as landmarks. White patches in RS represent overlap between M2 and callosally-projecting neurons. (C) M2 immunostaining in tangential section through layer 4 showing intense, uniform expression in V1. M2 expression in L4 of extrastriate visual cortex is less intense and uniform. Anterior area (A), anterolateral area (AL), auditory cortex (Au), anteromedial area (AM), entorhinal cortex (ENT), laterointermediate area (LI), lateromedial area (LM), mediomedial area (MM), posterior area (P), posteromedial area (PM), postrhinal area (POR), rostrolateral area (RL), retrosplenial cortex (RS), primary somatosensory area (S1), secondary somatosensory area (S2), temporal posterior area (TEp), primary visual area (V1). Axes: anterior (a), dorsal (d), lateral (l).
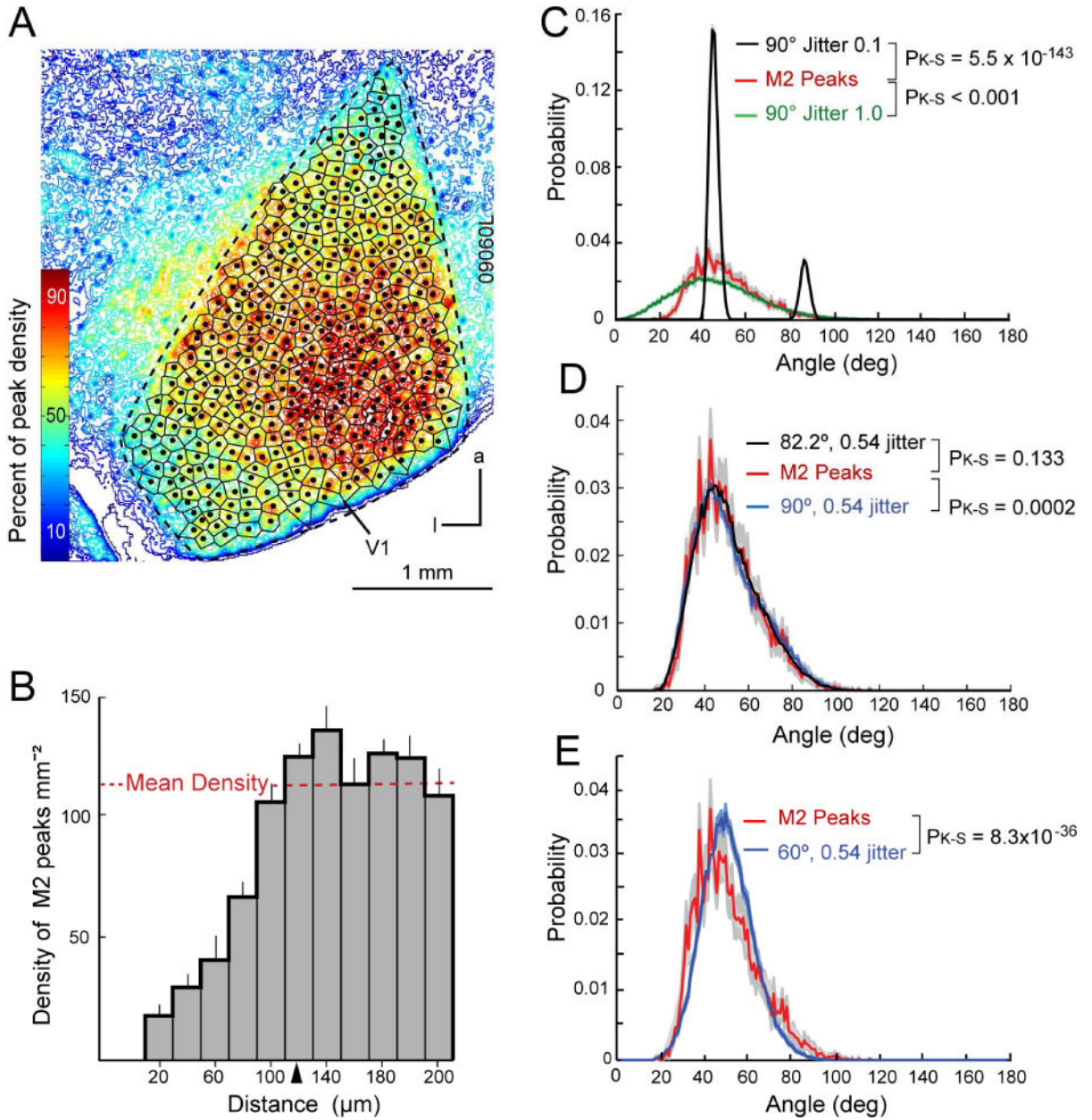
Figure 3. Non-random organization of M2 patches in L1 of mouse V1

(A) Optical density map of M2 expression in L1 of V1. Dots indicate centroids (M2 peaks) and are seed points for tessellation of V1 into Voronoi polygons. Notice that the absolute staining intensity across V1 differs, due to local variations in the plane of section, section thickness and staining intensity. However, the relative density of M2 expression between M2+ and M2− zones is roughly constant across V1. Anterior (a), lateral (l). (B) Density recovery profile of M2 peaks obtained by averaging measurements from 5 different cortices. The plot shows that the spatial density of M2 peaks equals the mean of a random distribution if the distance between centroids exceeds the effective radius of 120 μm. Peaks that are closer together and fall in the 'dead space' (<120 μm) are less common, indicating that they have a mosaic arrangement with a center-to-center spacing of 120 ± 3.6 μm. (C)

Interneighbor angle distributions of M2 peaks (red) ± SEM (grey) compared with nearly perfect square lattice (black, jitter 0.1) and a square lattice drawn from a Poisson distribution of seed points (green, jitter 1.0). $P_{k\text{-}s}$ indicates *p*-values obtained from comparisons with 2-sided Kolmogorov-Smirnov test. (D) Comparison of interneighbor angels showing that the measured angles between neighboring M2 patches (red) ± SEM (grey) differs from a rectangular lattice (blue) and corresponds best to a 82.2 deg lattice with 0.54 jitter (black). (E) Comparison of interneighbor angels shows that the angles between M2 patches (red) ± SEM (grey) differ from a hexagonal lattice with 0.54 jitter (blue).
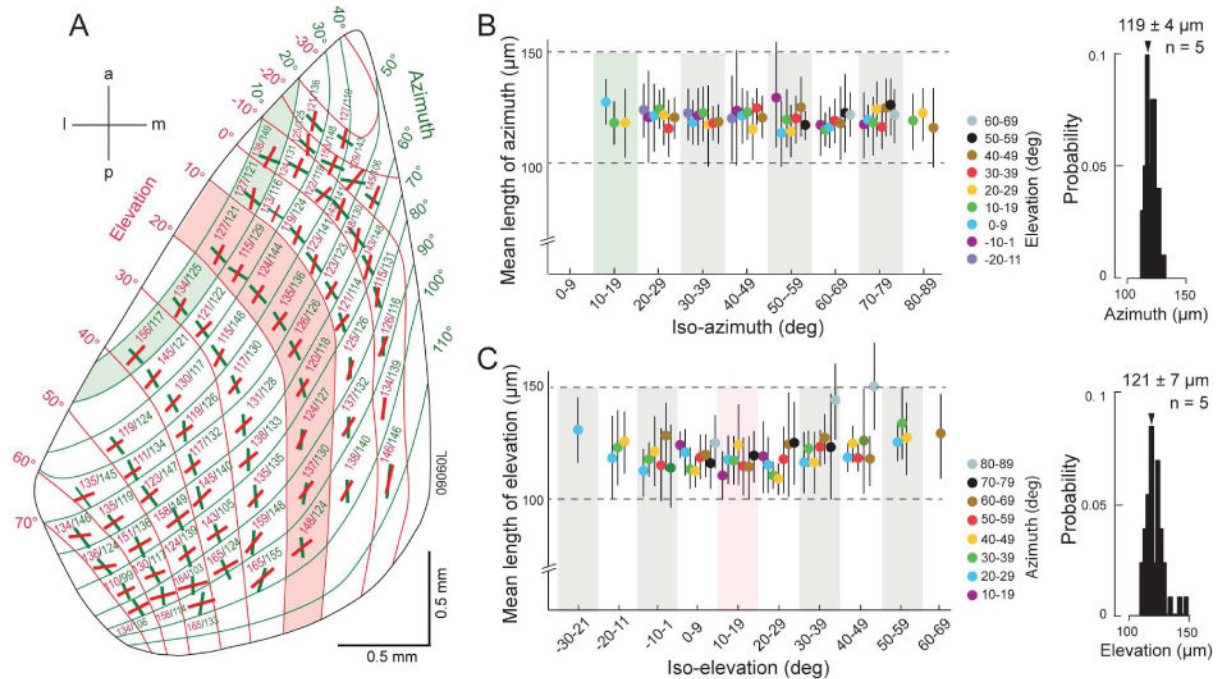
Figure 4. Constant-size domains across retinotopic map of mouse V1

(A) Mean axial lengths of domains contained within 10×10 deg tiles of the retinotopic map (Marshel et al., 2011). Red line segments denote elevation, green lines indicate azimuth. Red shading indicates iso-elevation band. Green marks iso-azimuth band. Anterior (a), medial (m), posterior (p), lateral (l). (B) Mean length of azimuth at different elevations across iso-azimuth bands. Green stripe indicates iso-azimuth band shown in (A). Azimuth is constant across all locations. Histogram shows the distribution of azimuth across the retinotopic map (mean ± SEM). (C) Mean length of elevation at different azimuths across iso-elevation bands. Red stripe corresponds to location of iso-elevation band shown in (A). Elevation is constant across all locations. Histogram shows the distribution of elevation across the retinotopic map (mean ± SEM).
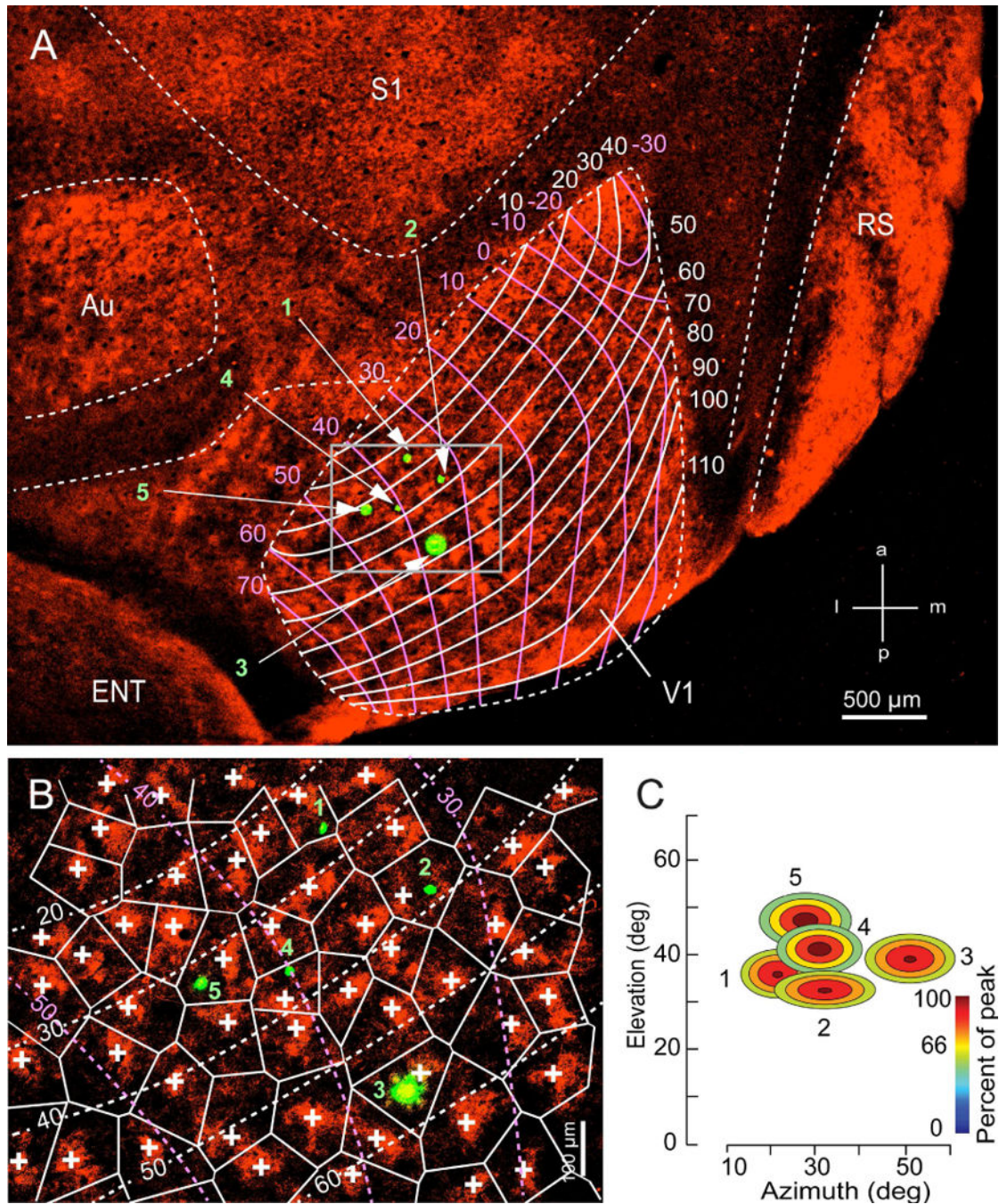
Figure 5. Domain size and retinotopic distance
A) Section through L1 of flatmounted occipital cortex stained with antibody against M2 (red). The grid represents the retinotopic map by Marshel et al., (2011). The cardinal axes are indicated by pink (elevation) and white (azimuth) lines. Green spots mark false colored DiI-labeled recording sites 1–5. Abbreviations same as in Figures 2 and 4. (B) Magnified image of boxed area in (A) tessellated into Voronoi polygons from seed points marked by M2 peaks (crosses). DiI-labeled recordings sites are false colored green. Notice that site 3 falls into M2+ zone, whereas sites 1, 4 and 5 mark M2– zones. Site 2 lies could not be

assigned with confidence. (C) Receptive fields after smoothing with Gaussian function. Yellow to brown colored area includes 66% of spike responses and marks the size of the RFs. Recording sites shown in (B) map different RF locations. Separation between non-overlapping RF is greater than diameter of domain.
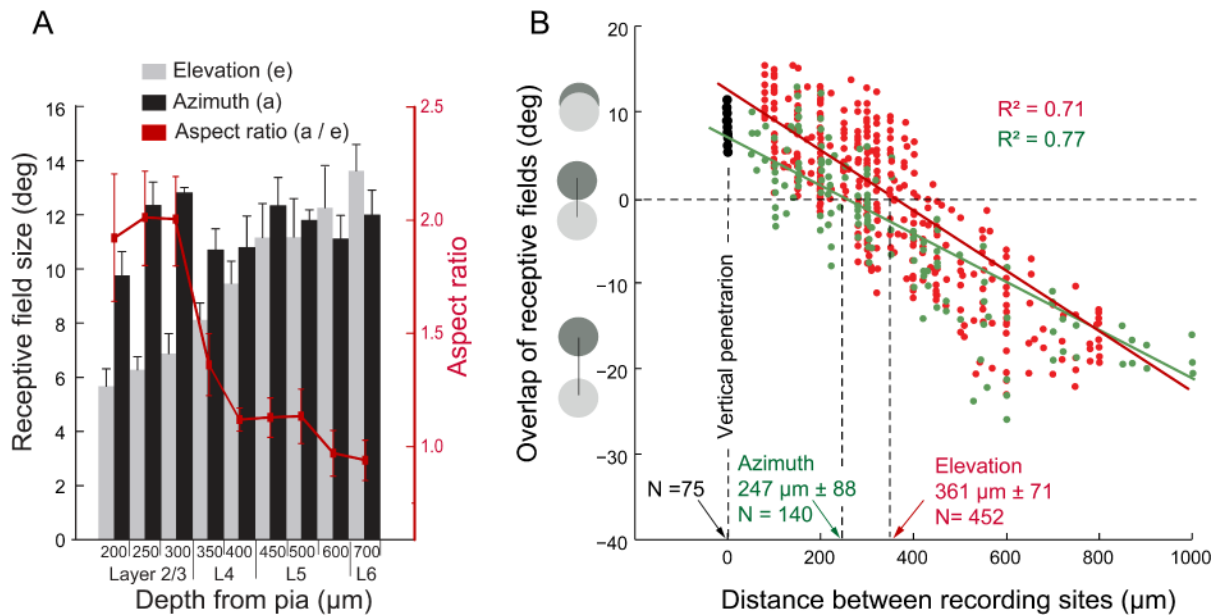
Figure 6. Size of the point image in mouse V1

(A) RFs smoothed by Gaussian filter are shaped elliptically. The anisotropy is most profound in L2 and L3 in which the azimuth (a, black) is double the length of elevation (e, gray). Red line indicates aspect ratio (a/e) which was similar in M2+ and M2− zones (data pooled). (B) RF-overlap as a function of tangential distance between recording sites. Black dots mark recordings on vertical tracks across L2-6. Notice that RFs are largely overlapping. RF-overlap in L2/3 decreases as the tangential separation between recording sites (azimuth = green, elevation = red) increases. Zero-crossings of the linear regression of RF-overlap indicate the tangential separation between recording sites representing adjacent, non-overlapping RFs. Notice that the zero-crossing for azimuth is smaller than for elevation, indicating that along both axes multiple ~120 μm-wide domains are contained within the point image. N = Number of comparisons.
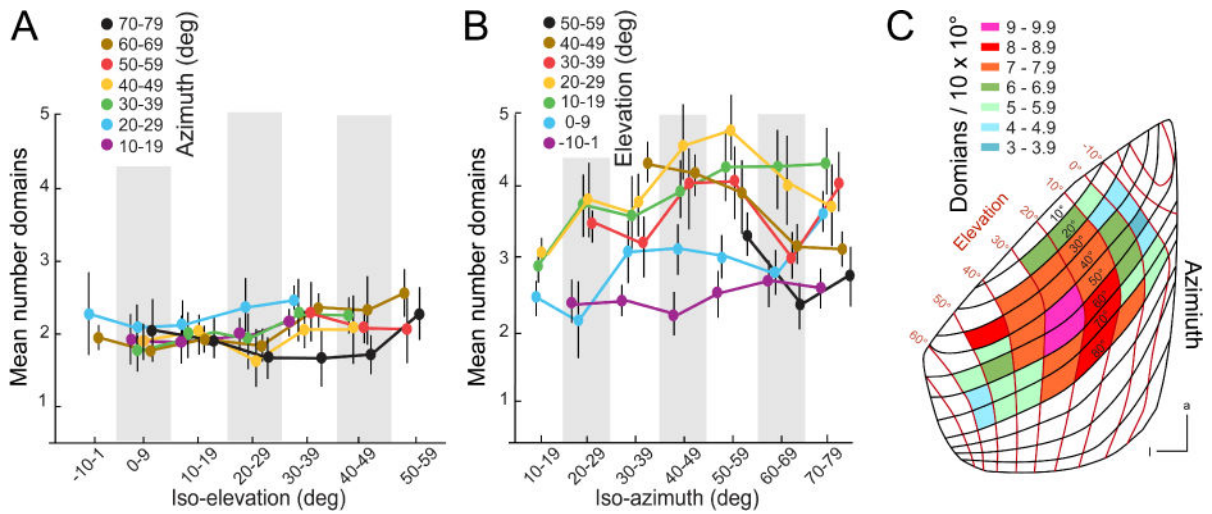
Figure 7. Number of domains across mouse V1
(A) Mean number of domains contained within 10 × 10 deg tiles across different azimuths within different iso-elevation bands is constant. (B) Mean number of domains contained within 10 × 10 deg tiles across different elevations within different iso-azimuth bands is constant near the horizontal meridian, but shows a peak in the upper visual field. (C) Distribution of the number of domains in 10 × 10 deg tiles across the retinotopic map. Notice that number of domains in the upper central visual field is increased. Anterior (a), lateral (l).
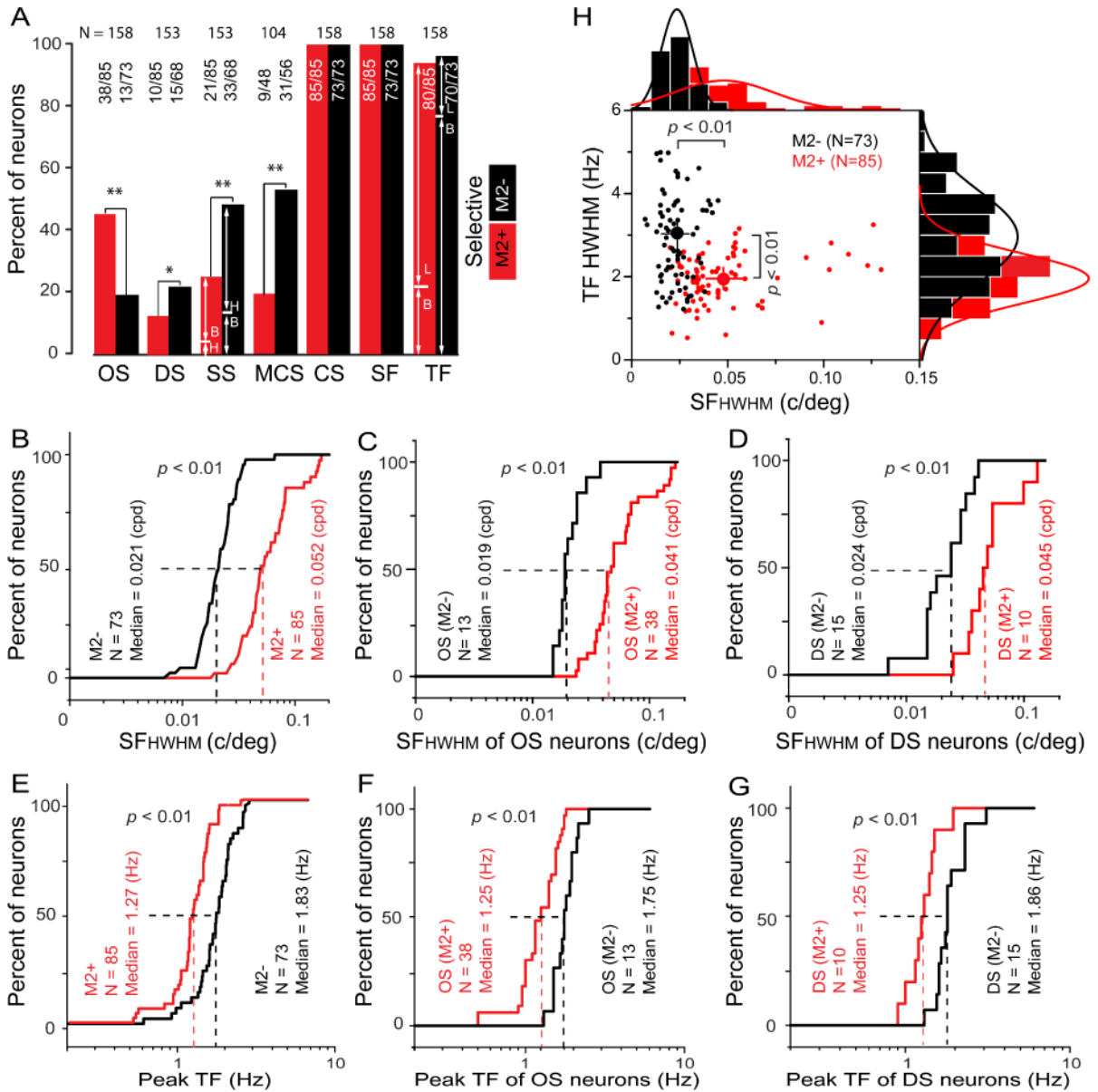
Figure 8. Different spatiotemporal sensitivities of L2/3 neurons aligned with M2+ and M2− zones in L1 of mouse V1

(A) Percent OS, DS, SS, MCS, CS, SF, TF in M2+ (red) and M2− (black) zones. OS neurons are 2.5-fold more frequent in M2+ zones, whereas DS is 1.8-fold, SS 2-fold and MCS is 2.9-fold more frequent in M2− zones. B: bandpass, H: highpass, L: lowpass. (B) Cumulative frequency plot of the total pool of neurons, showing that the median SF_{HWHM} is significantly higher in M2+ (red) than M2− zones (black). (C, D) Cumulative frequency plot of SF_{HWHM} of OS (C) and DS neurons (D), showing that high SF sensitivity is unrelated to OS or DS, but is specific to M2+ zones. (E) Cumulative frequency plot of the total pool of neurons, showing that the median TF peak is significantly lower in M2+ (red) than M2− zones (black). (F, G) Cumulative frequency plot of TF peak of OS (F) and DS neurons (G), showing that the high TF sensitivity is unrelated OS or DS, but is specific to M2− zones. (H) Cell-by-cell comparison of SF and TF sensitivities, showing that in M2+ zones (red) cells

with high SF sensitivity prefer low TF sensitivity, whereas cells in M2− zones (black) with low SF prefer high TF. Large dots indicate median values ± SEM.